



UNIVERSITY OF LEEDS

This is a repository copy of *Physical controls on the variability of offshore propagation of convection from Sumatra*.

White Rose Research Online URL for this paper:

<https://eprints.whiterose.ac.uk/id/eprint/225122/>

Version: Accepted Version

Article:

Peatman, S.C., Birch, C.E. orcid.org/0000-0001-9384-2810, Schwendike, J. et al. (5 more authors) (Accepted: 2025) Physical controls on the variability of offshore propagation of convection from Sumatra. *Journal of Geophysical Research: Atmospheres*. ISSN 2169-897X (In Press)

This is an author produced version of an article accepted for publication in *Journal of Geophysical Research: Atmospheres*, made available under the terms of the Creative Commons Attribution License (CC BY), which permits unrestricted use, distribution and reproduction in any medium, provided the original work is properly cited.

Reuse

This article is distributed under the terms of the Creative Commons Attribution (CC BY) licence. This licence allows you to distribute, remix, tweak, and build upon the work, even commercially, as long as you credit the authors for the original work. More information and the full terms of the licence here:

<https://creativecommons.org/licenses/>

Takedown

If you consider content in White Rose Research Online to be in breach of UK law, please notify us by emailing eprints@whiterose.ac.uk including the URL of the record and the reason for the withdrawal request.



eprints@whiterose.ac.uk
<https://eprints.whiterose.ac.uk/>

Physical controls on the variability of offshore propagation of convection from Sumatra

Simon C. Peatman^{1,2}, Cathryn E. Birch¹, Juliane Schwendike¹, John H. Marsham¹, Emma Howard^{3,4,5}, Steven J. Woolnough^{4,5}, Jack M. Mustafa^{1,6},
Adrian J. Matthews^{6,7}

¹Institute for Climate and Atmospheric Science, School of Earth and Environment, University of Leeds,
Leeds, United Kingdom

²Centre for Climate Research Singapore, Meteorological Service Singapore

³Bureau of Meteorology, Brisbane, Australia

⁴Department of Meteorology, University of Reading, Reading, UK

⁵National Centre for Atmospheric Science, University of Reading, Reading, UK

⁶Centre for Ocean and Atmospheric Sciences, School of Environmental Sciences, University of East
Anglia, Norwich, United Kingdom

⁷School of Mathematics, University of East Anglia, Norwich, United Kingdom

Key Points:

- The offshore propagation of convection south-west of Sumatra is a key feature of the mean diurnal cycle but occurs on only 28% of DJF days
- The diurnal cycle over land occurs when large-scale onshore wind causes convergence over the mountains and low-level humidity causes moist instability
- Offshore propagation arises due to the mid-level wind, convergence due to land breezes or cold pools, and inflow of low-level unstable air

Corresponding author: Simon Peatman, simon_peatman@nea.gov.sg

Abstract

Previous work has explained the physical mechanisms behind nocturnal offshore propagation of convection south-west of Sumatra. Low-level moisture flux convergence due to the land breeze front controls the progression of convection, typically a squall line, away from the coast overnight. However, the diurnal convection over the mountains occurs on only 57% of days in December–February (DJF) and propagates offshore on only 49% of those days. We investigate day-to-day variability in dynamical and thermodynamical conditions to explain the variability in diurnal convection and offshore propagation, using a convection-permitting simulation run for 900 DJF days. A convolutional neural network is used to identify regimes of diurnal cycle and offshore propagation behaviour. The diurnal cycle and offshore propagation are most likely to occur ahead of an active Madden-Julian Oscillation, or during El Niño or positive Indian Ocean Dipole; however, any regime can occur in any phase of these large-scale drivers, since the major control arises from the local scale. When the diurnal cycle of convection occurs over land, low-level wind is generally onshore, providing convergence over the mountains; and low-level humidity over the mountains is high enough to make the air column unstable for moist convection. When this convection propagates offshore, mid-level offshore winds provide a steering flow, combined with stronger convergence offshore due to more onshore environmental winds. Low-level moisture around the coast also means that, as the convection propagates, the storm-relative inflow of air into the system adds greater instability than would be the case on other days.

Plain Language Summary

In Sumatra, a large island of west Indonesia, rainfall tends to form by convection over the mountains during the afternoon and evening. This is known as the diurnal cycle. Furthermore, the rainfall often propagates overnight, both offshore (towards the south-west) and onshore (towards the north-east). A previous paper investigated the physics behind this offshore propagation; overnight the land breeze converges offshore with what remains of the sea breeze from earlier in the day, and the convergence of air masses causes uplift at the front between them, sustaining the line of convection which duly propagates offshore. However, neither the diurnal cycle nor its offshore propagation occur every day. This study investigates the physical conditions that control whether these phenomena occur on any given day. The Madden-Julian Oscillation, El Niño–Southern Oscillation

54 and Indian Ocean Dipole all have an impact, but they alone cannot predict if the diurnal
55 convection will occur or if it will propagate. Instead, these phenomena are controlled
56 by the wind direction and low-level humidity, which cause convergence of air over the
57 mountains and an unstable vertical profile when there is a diurnal cycle; and offshore mid-
58 level winds, convergence of air over the sea and inflow of unstable air when there is off-
59 shore propagation.

60 **1 Introduction**

61 Located in the Indo-Pacific warm pool, the Maritime Continent (the south-east Asia
62 archipelago; Ramage, 1968) experiences intense deep convection, with the diurnal cycle
63 being the greatest form of variability (e.g., Yang & Slingo, 2001; Qian, 2008; Biasutti et
64 al., 2012). Typically, the diurnal cycle of precipitation peaks over the islands during the
65 afternoon and evening, whereas over the sea the peak is during the early hours of the
66 morning. However, this diurnal cycle does not occur on all days and when it does oc-
67 cur the amplitude may vary considerably between days. Many studies have described
68 scale interactions in which the local-scale diurnal cycle is forced by large-scale weather
69 phenomena. For example, the strongest diurnal cycle tends to occur ahead of the arrival
70 of an active Madden-Julian Oscillation (MJO) envelope (Oh et al., 2012; Peatman et al.,
71 2014; Sakaeda et al., 2017; Vincent & Lane, 2017; Sakaeda et al., 2020; Peatman et al.,
72 2021); the El Niño–Southern Oscillation (ENSO) can enhance the local diurnal cycle of
73 rainfall over the islands in the El Niño phase, even though on the large scale the Mar-
74 itime Continent rainfall is suppressed (Rauniyar & Walsh, 2013); and previous studies
75 stated that the negative phase of the Indian Ocean Dipole (IOD) causes wetter extremes
76 (Kurniadi et al., 2021) and a stronger diurnal cycle over the southern half of Sumatra
77 (Fujita et al., 2013).

78 There is growing evidence that these scale interactions result, at least in part, from
79 the way in which large-scale drivers control coastal winds. Peatman et al. (2021) showed
80 that over south-west Sumatra a stronger diurnal cycle and stronger offshore propaga-
81 tion tend to occur when coastal winds are offshore, while strong onshore winds result in
82 a very weak diurnal cycle and no offshore propagation. Similar results were found for
83 offshore propagation from Borneo and Java. A more comprehensive study by Aoki and
84 Shige (2024) investigated precipitation rates and offshore propagation under onshore and
85 offshore wind conditions of varying strengths, across the global tropics. The Maritime

86 Continent experiences the most intense diurnal cycle of rainfall over land when daily mean
87 850 hPa wind is moderate or weak. Strong onshore winds (fifth panel of their figure 7e)
88 are associated with large-scale rain rather than a localized diurnal cycle, in agreement
89 with Peatman et al. (2021).

90 Over certain regions of the Maritime Continent, organized convection that is ini-
91 tiated over land is observed to propagate offshore overnight (e.g., Mori et al., 2004; Love
92 et al., 2011; Sakaeda et al., 2020; Peatman et al., 2023), including to the south-west of
93 Sumatra. Although the Hovmöller diagrams in Aoki and Shige (2024)'s figure 7 do not
94 show hours of the following day, so it is not possible to see nocturnal offshore propaga-
95 tion, the authors make further arguments relating to the Doppler shifting and advection
96 of gravity waves to explain an asymmetry between onshore and offshore propagation un-
97 der strong coastal wind conditions.

98 The physical mechanisms of the offshore propagation, in the Maritime Continent
99 and other tropical locations, have been investigated using both observations and mod-
100 els (Houze et al., 1981; Mapes, Warner, & Xu, 2003; Mapes, Warner, Xu, & Negri, 2003;
101 Love et al., 2011; Peatman et al., 2023). The proposed mechanism of Houze et al. (1981,
102 see their figure 16) for offshore propagation from Borneo involved low-level convergence
103 between a land breeze and the monsoon wind, triggering convection successively offshore.
104 On the other hand, Mapes, Warner, Xu, and Negri (2003) explained offshore propaga-
105 tion over the Panama Bight in terms of gravity waves emitted by the boundary layer trig-
106 gering offshore convection (see their figure 11). For south-west Sumatra, Love et al. (2011)
107 noted a transition from a convective profile with mid-tropospheric heating during early
108 afternoon to a stratiform profile with upper-tropospheric heating and mid-tropospheric
109 cooling at later times. They attributed the offshore propagation to gravity waves forced
110 by this change in the heating profile.

111 Peatman et al. (2023) considered the land-sea breeze circulation induced by the land-
112 sea temperature contrast and its effect on the propagation (see their figure 14). They
113 found that, in examples of clear and coherent propagation, a land breeze provides strong
114 low-level moisture flux convergence as it converges with the remnant of the onshore sea
115 breeze from earlier in the day. An organized squall line that forms over the Barisan moun-
116 tains, aligned along Sumatra's south-west coast, propagates offshore collocated with the
117 convergence line due to the land breeze. There may also have been a contribution to the

118 moisture flux convergence from cold pools caused by the convection, but it was not possible to disentangle this from the effect of the land breeze.
119

120 Furthermore, gravity waves propagating offshore can trigger isolated convection, which in a composite is averaged out to appear as a faster mode of propagation. However, Peatman et al. (2023) demonstrated that gravity waves are not responsible for the coherent, organized squall line which forms over the Sumatran mountains and propagates offshore as an organized system on any given day.
121
122
123
124

125 Although we know that the diurnal cycle and its offshore propagation vary according to the large scale, and we understand the physical mechanism of the offshore propagation when it occurs, there remains a lack of understanding of the physical mechanisms that cause the day-to-day variability in offshore propagation at the local scale. The present study addresses this by identifying a range of diurnal cycle and offshore propagation behaviours, and uses a convection-permitting simulation to understand the dynamical and thermodynamical conditions associated with each. We opt to use a convection-permitting model instead of a reanalysis for this research since reanalyses typically rely on convection parametrization schemes which may not represent the location and timing of convective storms correctly, and because running a model allows us to output a comprehensive set of diagnostics that we require.
126
127
128
129
130
131
132
133
134
135

136 The model and methodologies used are explained in section 2, results are presented in section 3 and a discussion is found in section 4.
137

138 **2 Data and methods**

139 **2.1 Observational data**

140 Gridded precipitation observations are taken from the Global Precipitation Measurement (GPM)'s Integrated Multi-satellitE Retrievals for GPM (IMERG) dataset, version 6 (Huffman et al., 2019), which is provided on a 0.1° grid every 30 minutes. The phase of the MJO for any given day is taken from the Real-time Multivariate MJO index (RMM; Webster & Hoyos, 2004), discarding days on which the RMM amplitude is less than 1 as the MJO is defined as being weak. Orography is shown using the Global Land One-km Base Elevation (GLOBE) project (Hastings et al., 1999).
141
142
143
144
145
146

147 The December to February (DJF) seasons used in this study (see section 2.2) were
 148 judged in table 1 of Howard et al. (2024) to belong, overall, to a particular phase of ENSO
 149 (El Niño, La Niña or neutral) using the Niño3.4 index; and the IOD (positive or neg-
 150 ative) using the Dipole Mode Index. These ENSO and IOD phases are used in the present
 151 study also.

152 **2.2 Convection-permitting MetUM simulation**

153 We use a convection-permitting configuration of the Met Office Unified Model (MetUM),
 154 which was described and evaluated by Howard et al. (2024), and is summarized here. The
 155 model setup is illustrated in figure 1. The outer domain is 85–160°E and 20°S–20°N, with
 156 a 0.09375° (latitude) by 0.140625° (longitude) grid, equating to approximately 12 km grid
 157 spacing at the equator. At the lateral boundaries, forcing is provided by the European
 158 Centre for Medium-Range Weather Forecasting (ECMWF) Reanalysis 5 (ERA5; Hers-
 159 bach et al., 2020), every 6 hours. This 12 km model has parametrized convection.

160 The nested inner domain is 90–155°E and 15°S–15°N, with a 0.02° grid, equating
 161 to approximately 2.2 km grid spacing at the equator; and is driven at the lateral bound-
 162 aries by the 12 km model. This 2.2 km model has explicit convection and uses the trop-
 163 ical version of the Regional Atmosphere and Land 2 (RAL2T) science configuration (Bush
 164 et al., 2023).

165 Both atmospheric models are coupled to a *K*-Profile Parameterisation (KPP) ocean
 166 model (Large et al., 1994) on the same horizontal grid as the 12 km configuration. This
 167 is a mixed-layer model – that is, all columns are independent one-dimensional models
 168 simulating vertical mixing but there is no horizontal transport, allowing the represen-
 169 tation of air-sea interactions with little computational expense.

170 Only the 2.2 km convection-permitting model is used in the present study, with out-
 171 put available up to every 5 minutes.

172 The model was run for 10 DJFs, chosen to cover a range of large-scale conditions,
 173 including different phases of ENSO and the IOD, and different levels of MJO activity.
 174 For details, see table 1 of Howard et al. (2024). For consistency, these same 10 DJFs were
 175 used for all observational parts of the present study.

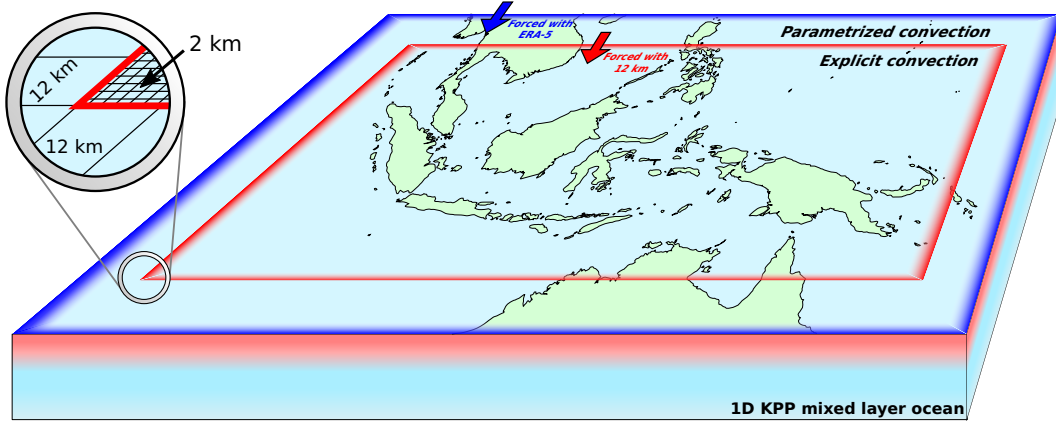


Figure 1. Schematic diagram of the MetUM simulation used in this study. For more details, see Howard et al. (2024).

176 Note that the MetUM run is used as a research tool to investigate the physical mech-
 177 anisms of the diurnal cycle of convection and its propagation, not as a forecast tool. There-
 178 fore, the days on which the diurnal convection occurs over Sumatra and the days on which
 179 it propagates offshore may differ between the model and observations, but this is not a
 180 problem provided the model has a reasonably realistic distribution of diurnal cycle be-
 181 haviour. Due to forcing at the boundaries by ERA5, large-scale phenomena should be
 182 represented with a high degree of accuracy (see Howard et al., 2024, for details), but on
 183 the local scale we do not expect such a strong match with the observations.

184 **2.3 Subjective classification of propagation regimes**

185 In order to investigate the day-to-day variability in offshore propagation, Hovmöller
 186 diagrams of observed precipitation from IMERG were created, using the red box in fig-
 187 ure 2, averaging over the long side. This was done for the same 900 days as were cov-
 188 ered by the MetUM simulation. Eight examples are shown in figure 3.

189 A visual inspection of the 900 Hovmöllers suggested four broad regimes, listed in
 190 table 1. The examples in figure 3 include two instances of each regime, indicated by the
 191 coloured rectangles above the panels. When there is a diurnal cycle of convection, with
 192 precipitation peaking over the mountains in the late afternoon or evening, the precip-
 193 itation may (figures 3c,f,h) or may not (figure 3g) propagate onshore, north-eastward.
 194 However, we focus solely on the propagation to the south-west in this study.

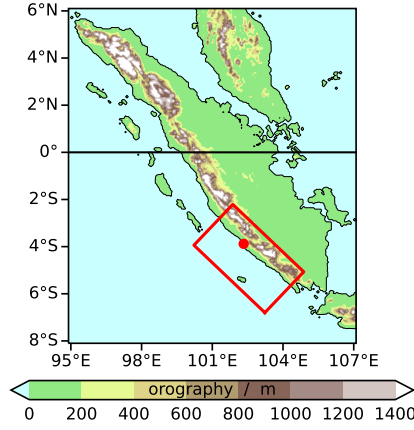


Figure 2. Orography of Sumatra from the GLOBE dataset, with the Hovmöller box used in figures 3 and 4 drawn in red. The red dot is Bengkulu.

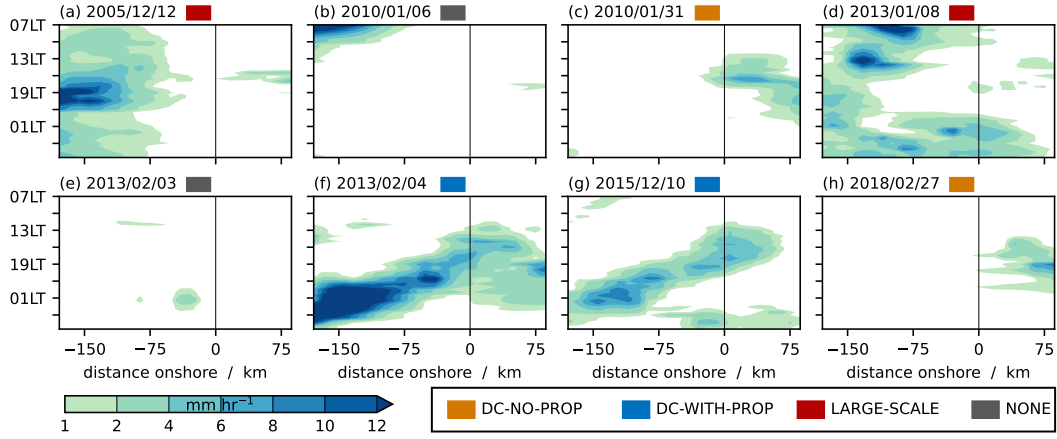


Figure 3. Example offshore-propagating Hovmöller diagrams of precipitation from IMERG observations for the red box shown in figure 2, averaged over the alongshore direction, with local time (LT) running down the page from 07 LT one day to 07 LT the next. The black vertical line at $x = 0$ is the south-west coast of Sumatra, with the land, mainly covered by mountains, to the right ($x > 0$) and the sea to the left ($x < 0$). Eight selected days are shown, from within the model run period. Coloured rectangles indicate the regime for the day shown (see section 2.3 and table 1).

195 The 900 Hovmöller diagrams were each classified subjectively as belonging to one
 196 of the four regimes. In order to achieve a degree of robustness, this exercise was performed
 197 independently by two of the authors. Where they agreed on the classification (which was
 198 true for 701 of the days), this classification was taken as definitive. For the remaining
 199 199 days, the process was repeated until a majority verdict was reached.

Table 1. Names of regimes found in Hovmöllers of precipitation and a description of each.

Regime	Description
DC-NO-PROP	Diurnal cycle of precipitation occurs over mountains but precipitation does not propagate offshore*
DC-WITH-PROP	Diurnal cycle of precipitation occurs over mountains and precipitation does propagate offshore
LARGE-SCALE	Hovmöller is dominated by large-scale rainfall for much or all of the day
NONE	None of the above – very little or no rainfall

*This does not necessarily preclude precipitation propagating onshore, to the north-east.

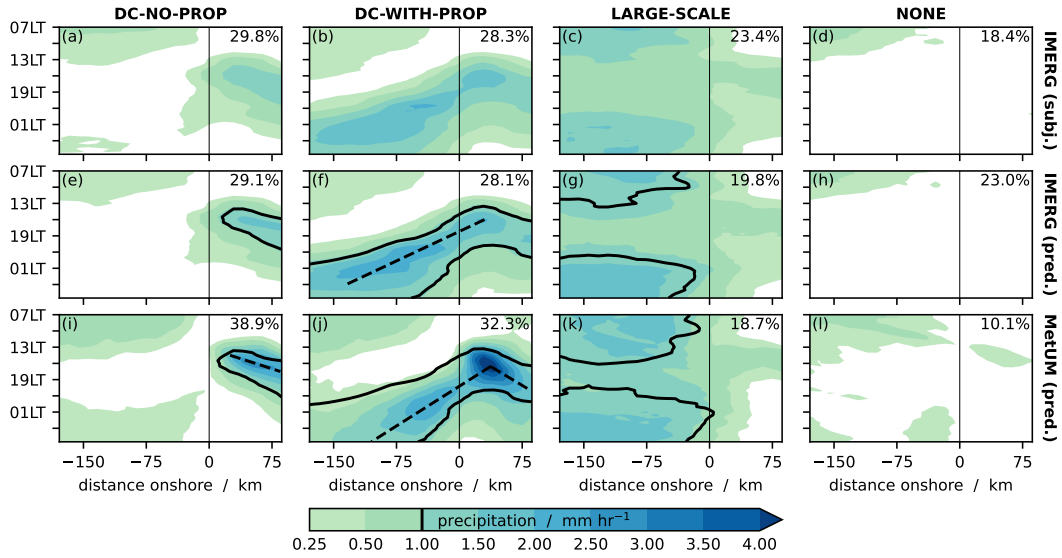


Figure 4. Composite Hovmöller diagrams of precipitation for (a–d) IMERG (subjective classification), (e–h) IMERG (CNN-predicted) and (i–l) the MetUM simulation (CNN-predicted). Numbers in the top-right of each panel indicate the percentage of days in that regime. The black 1 mm hr⁻¹ contour in (e–h) is taken from the shading in (a–d), and in (i–l) is taken from the shading in (e–h), for comparison. The black dashed lines indicate propagation at (f) 3.8 m s⁻¹ offshore, (i) 5.6 m s⁻¹ onshore, and (j) 2.8 m s⁻¹ offshore and 3.0 m s⁻¹ onshore.

200

2.4 Supervised machine learning

201

202

While the observations were classified into regimes subjectively (section 2.3), for consistency and convenience this process was automated for the MetUM output, using

203 the subjective classifications from the observations to train a supervised machine learn-
 204 ing model.

205 A convolutional neural network (CNN) was used with the architecture shown in
 206 figure S1. 75% of the observations (675 days) were randomly selected as the training data
 207 set and the remaining 25% (225 days) formed the testing data set. Hovmöller diagrams
 208 as in figure 3 were used as input images and the subjectively-classified regimes, to be pre-
 209 dicted by the CNN, were represented as one-hot vectors. Prior to training, the training
 210 data were augmented by randomly rotating images by up to 20°, or randomly translat-
 211 ing them either horizontally or vertically by up to 10%. Data augmentation (e.g., Montser-
 212 rat et al., 2017; Shorten & Khoshgoftaar, 2019; Poojary et al., 2021) gives greater scope
 213 for the CNN to recognize patterns that are not at exactly the same orientation or in ex-
 214 actly the same place as in the 675 input Hovmöllers used.

215 For the subjective classification in section 2.3 the images were not normalized first,
 216 so the images were also not normalized in the CNN. Hence, the CNN makes its predic-
 217 tions based on the magnitude of the precipitation as well as its spatial pattern.

218 Repeating the creation and training of a CNN will not produce an identical result,
 219 owing to the randomness in the selection of the training data set, the data augmenta-
 220 tion, the initialisation of the CNN’s hyperparameters and the batching of input data dur-
 221 ing training. 50 separate CNNs were trained and saved. The CNN with the highest ac-
 222 curacy where the accuracy (0.845) was approximately equal to validation accuracy (0.844)
 223 was chosen and the remaining CNNs were discarded. By way of comparison, the high-
 224 est accuracy achieved by any of the 50 CNNs was 0.869, but the validation accuracy was
 225 only 0.769 so it was likely overfitting to the training data set.

226 The CNN produces outputs x_0, \dots, x_3 (figure S1k), each in the interval $[0, 1]$ and
 227 with $\sum_i x_i = 1$. The largest of these determines the predicted regime (figure S1l). Some
 228 input images are classified with low certainty (i.e., $\max(x_i)$ is not close to 1), but it is
 229 difficult to quantify the degree of certainty since x_i cannot be interpreted as probabilit-
 230 ies (the CNN is not so calibrated). When classifying the observed Hovmöllers subjec-
 231 tively (section 2.3), the two people performing the classifications agreed at the first at-
 232 tempt on 701 occasions out of 900. We take this as an estimate of how certain we can
 233 reasonably expect a classification to be. Therefore, of all 900 of the $\max(x_i)$ values found
 234 when the CNN classified the observed Hovmöllers, the 701st largest value was taken as

235 a threshold. For any input image where the CNN’s $\max(x_i)$ is below this threshold, the
 236 classification is deemed uncertain.

237 Composites over each of the four regimes in observations are shown in figures 4a–
 238 d. The diurnal cycle of convection occurs over the mountains on just over 58% of DJF
 239 days, with a little under half of these having offshore propagation. The diurnal precip-
 240 itation and its offshore propagation show up clearly in long-term composites of the di-
 241 urnal cycle (e.g., Peatman et al., 2014) so this is typically thought of as the canonical
 242 behaviour for Sumatra and the sea to its south-west, but in fact this occurs on only around
 243 28% of DJF days. Composites for the 701 days with certain classifications are shown in
 244 figures 4e–h. When classifying the MetUM Hovmöllers, 749 days were above the thresh-
 245 old; composites for these days are in figures 4i–l.

246 The confusion matrix in figure 5a measures the performance of the CNN by compar-
 247 ing the subjectively-classified regimes and CNN-predicted regimes, both in observa-
 248 tions. If the CNN were perfect, all values would lie on the leading diagonal. With very
 249 few values off this leading diagonal, and with the composite Hovmöllers in figures 4e–
 250 h being very similar to those in figures 4a–d, we conclude that the CNN is successful in
 251 performing the classifications.

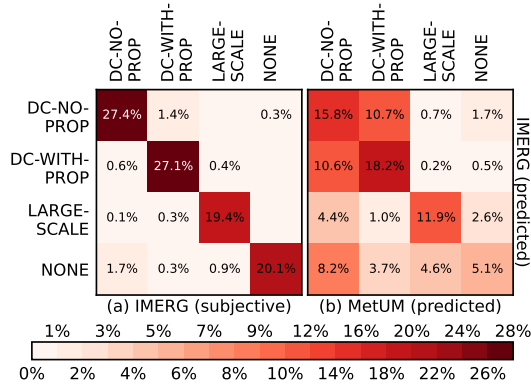


Figure 5. Confusion matrices showing (a) the performance of the CNN in classifying IMERG observations, compared against the subjective classification; (b) the performance of the MetUM simulation at producing days in the same regime as observations.

3 Results

3.1 Evaluation of MetUM simulation

Figures 4i–l show composite Hovmöller diagrams for each regime in the MetUM simulation. By construction there must be a degree of similarity with the observed composites in figures 4e–h, since the CNN seeks similar patterns of pixels in order to perform the classification. However, their remarkable similarity indicates that the model reproduces the observed regimes realistically. In figure 4i there is precipitation offshore overnight (bottom-left of panel) which is not seen in the corresponding figure 4e. This suggests there are MetUM days classified as DC-NO-PROP which could perhaps have been considered DC-WITH-PROP, but the offshore precipitation was too weak to be picked up by the CNN. In the DC-WITH-PROP regime, the modelled offshore propagation (2.8 m s^{-1}) is slightly slower than in observations (3.8 m s^{-1}).

The confusion matrix in figure 5b measures the performance of the MetUM simulation by comparing the regimes against observations, for those days when the CNN was above the certainty threshold for both. If the regime in the MetUM matched that in observations on all days, all values would lie on the leading diagonal.

The percentage of days falling into each regime are broadly similar for the observations and the model (figures 4e–l). The exception is that the NONE regime occurs less frequently in the model (10.1%; figure 4l) than in observations (23.0%; figure 4h), with the model instead having the two diurnal cycle regimes more often. Hence, in the MetUM the diurnal convection over the Sumatra mountains is triggered more often than in observations. When NONE occurs in observations, the MetUM may exhibit any of the other three regimes (bottom row of figure 5b).

The MetUM generally reproduces the LARGE-SCALE regime on the same days as observations. This is likely to be because the LARGE-SCALE regime arises from certain large-scale conditions in the region, and these should match well between the MetUM and observations due to the forcing at the lateral boundaries with ERA5. Looking at the four squares in the top-left of figure 5b, when the observations are in one of DC-NO-PROP or DC-WITH-PROP, the MetUM also tends to be in one of those two regimes. In other words, there is a good match in terms of whether the diurnal cycle of precipitation occurs. However, there is no close match between those two regimes, so the model does not

283 closely replicate the observed occurrence of offshore propagation on any given day. This
 284 suggests that the triggering of diurnal cycle rainfall may be more related to large-scale
 285 conditions, while the offshore propagation may depend more on localized conditions that
 286 are not reproduced realistically at a location far from the lateral boundary forcing.

287 **3.2 Dependence on large-scale drivers**

288 Previous studies have shown that the amplitude of the diurnal cycle varies through
 289 an MJO cycle (see section 1; Oh et al., 2012; Peatman et al., 2014; Sakaeda et al., 2017;
 290 Vincent & Lane, 2017; Sakaeda et al., 2020; Peatman et al., 2021), so we now examine
 291 the frequency of occurrence of each regime by MJO phase (figures 6a–d). LARGE-SCALE
 292 has a strong peak in phases 4–5, when the active MJO is over the Maritime Continent,
 293 which is consistent with large-scale convection being present. The diurnal cycle regimes
 294 tend to occur during the suppressed and pre-active phases, 7–2 for DC-NO-PROP and 8–
 295 2 for DC-WITH-PROP. NONE occurs fairly frequently during phases 4–5, so in an active
 296 MJO environment the diurnal cycle tends to be suppressed even if the large-scale rain-
 297 fall is weak or absent over this particular region on a given day; but NONE occurs most
 298 frequently in phase 6, just after the active envelope has passed through (the pre-suppression
 299 phase). These results are all consistent with Peatman et al. (2014), which found that the
 300 diurnal cycle has its greatest amplitude just ahead of the arrival of the large-scale ac-
 301 tive MJO envelope and is most strongly suppressed just ahead of the large-scale suppressed
 302 MJO conditions. However, note that here we find that all regimes can occur in all MJO
 303 phases, so the MJO does not uniquely determine the regime.

304 Convection over the Maritime Continent, on the large scale, tends to be enhanced
 305 during La Niña, due to the enhancement of the zonal Walker circulation, and suppressed
 306 during the opposite El Niño phase (e.g., Hendon, 2003). Moreover, Peatman et al. (2021)
 307 found that ENSO phase affects the diurnal cycle and offshore propagation for Sumatra,
 308 both being more enhanced during El Niño. Figures 6i–l are consistent with these find-
 309 ings, with El Niño favouring the diurnal cycle regimes and La Niña the LARGE-SCALE
 310 regime. ENSO is correlated with IOD, with El Niño most likely to coincide with IOD+
 311 and La Niña with IOD– (e.g., Stuecker et al., 2017). This is consistent with figures 6q–
 312 t, histograms of regimes by IOD phase, which show a similarity between the results for
 313 El Niño and IOD+, and La Niña and IOD–.

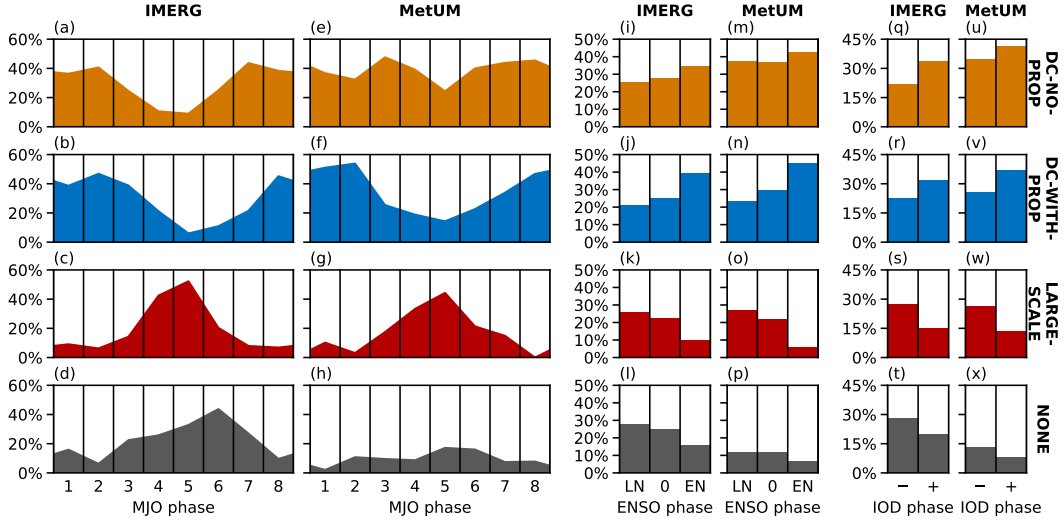


Figure 6. (a–h) For each MJO phase, the percentage of days that fall into each regime. (i–p) Similarly but for ENSO phase (La Niña, LN; neutral phase, 0; and El Niño, EN). (q–x) Similarly but for IOD phase. For each large-scale driver, the first column (a–d, i–l, q–t) is for IMERG observations and the second (e–h, m–p, u–x) for the MetUM simulation.

314 The remaining panels of figure 6 show equivalent results for the MetUM. For each
 315 large-scale driver the results for DC-WITH-PROP and LARGE-SCALE are very similar to
 316 the observations. As seen in section 3.1, the MetUM has far too few days in the NONE
 317 regime. Here we see that the dearth of NONE days (figure 6h) occurs as a result of ac-
 318 tive and pre-suppressed MJO days (phases 4–7), when the model is more likely to pro-
 319 duce DC-NO-PROP, hence the DC-NO-PROP histogram (figure 6e) failing to reproduce a
 320 broad minimum for the active phases, as seen in observations (figure 6a). However, the
 321 lack of NONE days and corresponding surfeit of DC-NO-PROP days have no strong depen-
 322 dence on phase when it comes to ENSO or the IOD.

323 3.3 Physical mechanisms responsible for the diurnal cycle

324 We now consider the dynamical and thermodynamical conditions that control which
 325 of the four regimes a given day falls into. For this we necessarily use only the MetUM
 326 simulations. As mentioned in section 1, although there has been much discussion in the
 327 literature regarding the role of gravity waves in the offshore propagation, earlier work
 328 (Peatman et al., 2023) showed that gravity waves do not play a primary role in the prop-

329 agation of the organized convection, so here we focus on the mechanism that the latter
 330 study found to be most important.

331 In figures 7a–d are composite maps of the dynamical conditions for each regime at
 332 13 LT. This time was chosen as the earliest time in the day at which the composites clearly
 333 differentiate the precipitation patterns between all regimes. In the two diurnal cycle regimes,
 334 convection has already been triggered over the mountains and is precipitating; in LARGE-
 335 SCALE, precipitation exceeding 1 mm hr^{-1} already covers all of the sea in the domain
 336 shown, but there is no triggering of convection over the mountains; and in NONE there
 337 is almost no precipitation.

338 The mean 10 m wind over the low-lying land (on the north-east side of the island
 339 – see figure 2) is very similar in all regimes, with predominantly north-westerly flow. How-
 340 ever, to the south-west of Sumatra, LARGE-SCALE and NONE have strong alongshore (north-
 341 westerly) flow, while the diurnal cycle regimes have much weaker large-scale flow and a
 342 sea breeze blowing approximately perpendicular to the coast. This causes low-level con-
 343 vergence over the mountains, seen as a coherent blue region in figures 7a,b and collocated
 344 with the diurnal cycle convection. In LARGE-SCALE and NONE the convergence over the
 345 mountains is weak and less coherent, contributing to the lack of convection there.

346 To investigate the thermodynamical conditions we use a moist instability diagnos-
 347 tic, $\theta_e^{300\text{m}} - \theta_{es}^{4500\text{m}}$ (e.g., Birch et al., 2016), where θ_e is equivalent potential temper-
 348 ature, θ_{es} is saturation equivalent potential temperature and heights are measured above
 349 the ground. The definition of θ_e is

$$\theta_e = \left(\frac{p_0}{p}\right)^{2/7} T_e \quad (1)$$

$$= \left(\frac{p_0}{p}\right)^{2/7} \left(T + \frac{rL_v}{c_{pd}}\right), \quad (2)$$

350 where T_e is equivalent temperature (the temperature that an air parcel would have if all
 351 water vapour were condensed out and the resulting latent heat used to heat the air par-
 352 cel), p is pressure, p_0 is a reference pressure (taken to be 1000 hPa), T is temperature,
 353 r is humidity mixing ratio, L_v is the latent heat of vaporization of water and c_{pd} is the
 354 specific heat capacity of dry air at constant pressure.

355 $\theta_e^{300\text{m}} - \theta_{es}^{4500\text{m}}$ is an approximate indicator of potential for moist convection (e.g.,
 356 Garcia-Carreras et al., 2011). Consider an air parcel at low levels (taken here to be 300 m
 357 above the ground). If this parcel were lifted pseudo-adiabatically to a mid-tropospheric

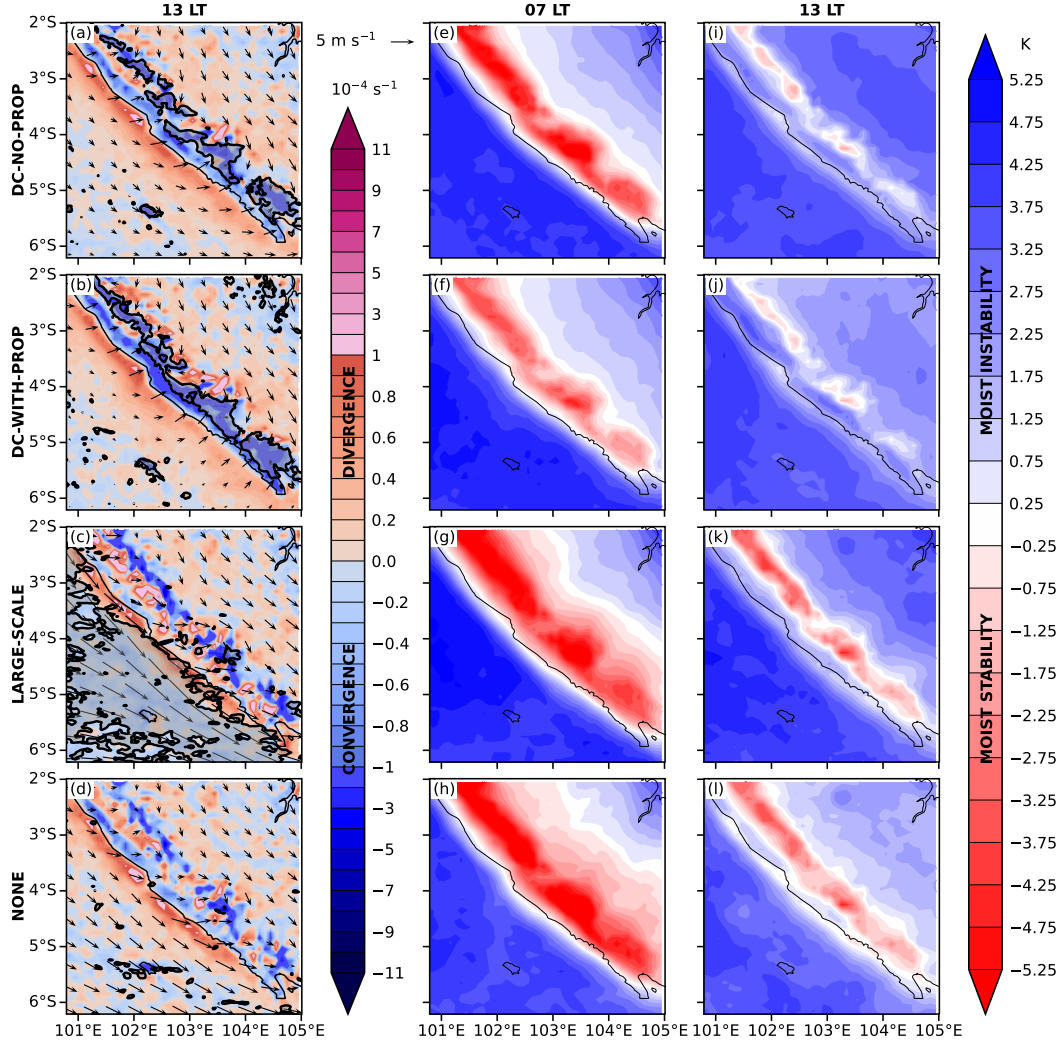


Figure 7. Composite maps at given times for each of the regimes. (a–d) Wind at 10 m (vectors), divergence at 10 m (coloured shading) and precipitation (black contour and transparent grey shading, 1 mm hr⁻¹), at 13 LT. (e–h) $\theta_e^{300m} - \theta_{es}^{4500m}$ at 07 LT. (i–l) As (e–h) but for 13 LT.

358

level where it is bound to be saturated (taken here to be 4500 m) and at that stage it still has positive buoyancy, we can expect it to continue rising and cause deep convection. Hence, the presence of moist instability is suggested by $\theta_e^{300m} > \theta_{es}^{4500m}$, or the diagnostic being positive (blue in figures 7e–l).

359

360

361

362

At both times of day shown, there is large-scale moist instability over the ocean and low-lying land in all four regimes. However, this does not necessarily cause convection to occur in these places, as there is also convective inhibition to be overcome (al-

363

364

365 though note that the instability is strongest in LARGE-SCALE, particularly at 07 LT, in
 366 which regime there is indeed rainfall over a wide area). In all regimes there is stability
 367 over the mountains at 07 LT, before the onset of diurnally-driven rainfall, although it
 368 is weaker in DC-WITH-PROP. By 13 LT the sign of the diagnostic has changed over al-
 369 most all of the mountains in the diurnal cycle regimes, and convection has duly occurred
 370 there. In LARGE-SCALE and NONE, even by this time of day, the atmospheric column is
 371 still stable against moist convection, hence the diurnal cycle of convection does not take
 372 place.

373 This raises the question of what causes the differences in $\theta_e^{300\text{m}} - \theta_{es}^{4500\text{m}}$ over
 374 the mountains, between the regimes. The mean diurnal cycle of this diagnostic, averaged
 375 over the mountains, is plotted in figure 8a. This confirms the distinction between i) the
 376 diurnal cycle regimes, where the diagnostic is positive from around 11:30 LT to around
 377 20:00 LT; and ii) LARGE-SCALE and NONE, where the atmospheric column is stable all
 378 day.

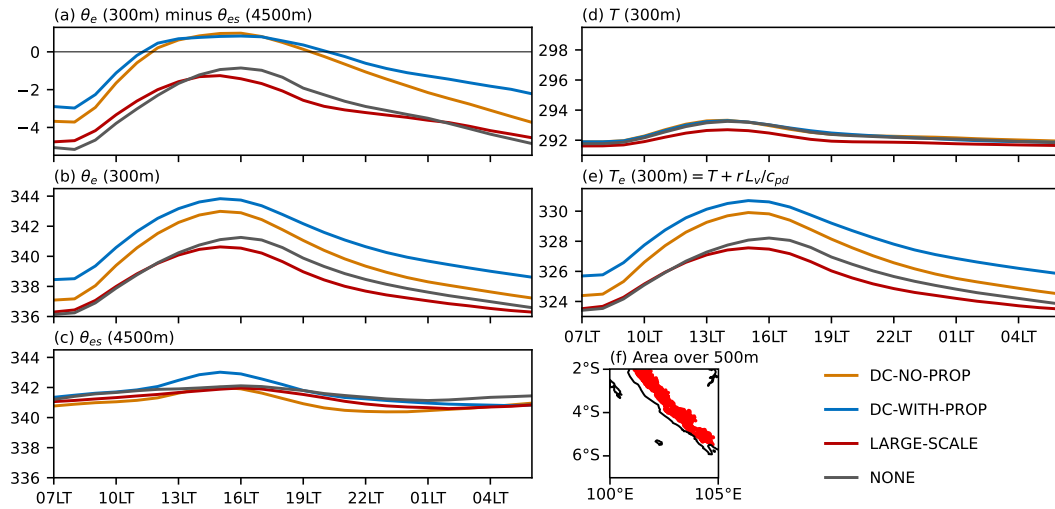


Figure 8. (a–e) Mean diurnal cycles in kelvin, averaged over land greater than 500 m above sea level, for each regime. (a) The moist instability diagnostic $\theta_e^{300\text{m}} - \theta_{es}^{4500\text{m}}$ (where heights are measured above the ground); (b) equivalent potential temperature, $\theta_e^{300\text{m}}$; (c) saturation equivalent potential temperature, $\theta_{es}^{4500\text{m}}$; (d) temperature, T ; (e) equivalent temperature, T_e , which is the sum of the temperature in panel (d) and a moisture term rL_v/c_{pd} . Note that panels (b) and (c) have the same vertical scale, and the vertical axes of panels (d) and (e) cover the same size range. (f) Map of the area over 500 m above sea level, over which quantities are averaged.

379 The mean diurnal cycle of each term is shown in figures 8b ($\theta_e^{300\text{m}}$) and 8c ($\theta_{es}^{4500\text{m}}$).
 380 The diurnal variability and the variability between regimes are dominated by $\theta_e^{300\text{m}}$, so
 381 it is the low-level conditions that dictate the instability, not the mid-level. We next ask
 382 what controls the value of $\theta_e^{300\text{m}}$. This is a function of T_e and p (equation 1). However,
 383 the variation in pressure is small enough to have negligible impact on the θ_e (not shown),
 384 so the problem reduces to explaining the variability in T_e .

385 The mean diurnal cycles of T and T_e are shown in figures 8d,e. A visual compar-
 386 ison of figures 8b and 8e shows that they are almost identical in shape, the only differ-
 387 ence being the factor of $(p_0/p)^{2/7}$ in the definition of potential temperature (equation 1),
 388 confirming that the variation in pressure between the regimes is negligible. Comparing
 389 T and T_e (the two panels have vertical scales covering the same size range), we see that
 390 for T both the diurnal variability and the variability between regimes are relatively small.
 391 Hence, it is the moisture term rL_v/c_{pd} present in figure 8e (see equation 2) that dom-
 392 inates.

393 Hence, it is variations in low-level humidity that control moist instability over the
 394 mountains; and, therefore, it is a combination of the sea breeze (causing convergence)
 395 and low-level humidity that cause the diurnal cycle of rainfall to occur.

396 **3.4 Physical mechanisms responsible for the offshore propagation**

397 The dynamical and thermodynamical conditions discussed in the previous section
 398 were used to explain the causes of the diurnal cycle regimes *versus* LARGE-SCALE and
 399 NONE; but those conditions, at the times of day considered thus far, do not explain the
 400 causes of DC-NO-PROP *versus* DC-WITH-PROP. Although there are very slight differences
 401 in the location of the precipitation over the mountains at 13 LT (figures 7a,b), with pre-
 402 cipitation having formed slightly closer to the coast in DC-WITH-PROP, the substantial
 403 differences between the two regimes emerge in the afternoon and evening. Figure 9 shows
 404 the dynamical conditions at 18 LT, by which time the difference in propagation behaviour
 405 is evident; and at 23 LT, by which time the precipitation in DC-WITH-PROP has extended
 406 tens of km offshore.

407 The 500 hPa winds at 18 LT (figure 10) are mostly westerly in DC-NO-PROP but
 408 mostly northerly in DC-WITH-PROP. These mid-level winds conceivably may steer the
 409 organized convection through advection. This is consistent with the differences between

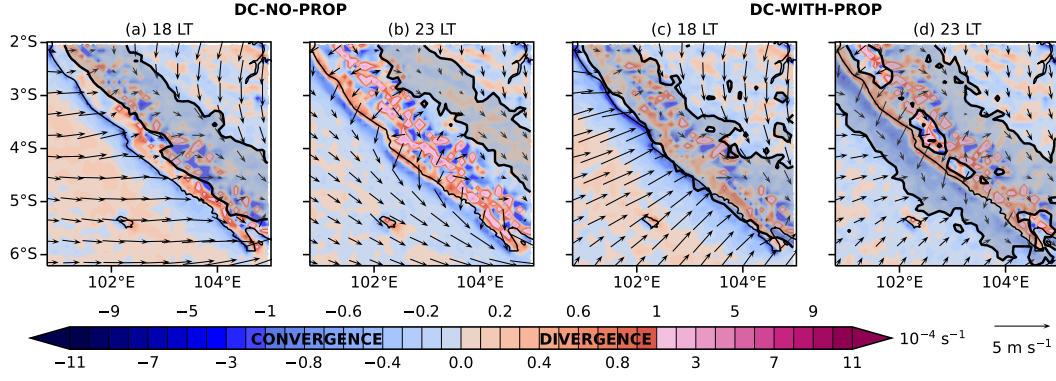


Figure 9. As figures 7a,b but for (a,c) 18 LT and (b,d) 23 LT. The black contour with transparent grey shading is precipitation (1 mm hr^{-1}).

410
411

figures 9a and 9c, which show that by 18 LT the precipitation has spread as far as the coast in DC-WITH-PROP, with no equivalent propagation in DC-NO-PROP.

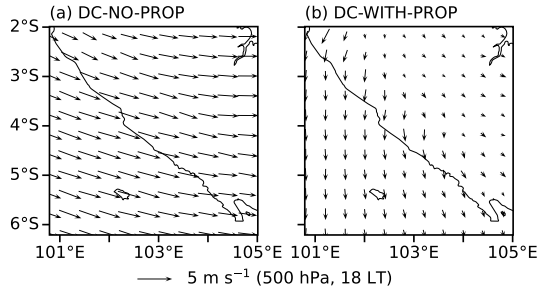


Figure 10. Composite wind at 500 hPa at 18 LT for days with a diurnal cycle (a) and no offshore propagation, and (b) with offshore propagation.

412
413
414
415
416
417
418
419
420
421

However, for the squall line to continue propagating for several hours, as is observed in DC-WITH-PROP, it is also necessary for the local conditions to sustain the deep convection. In section 1 it was explained that Peatman et al. (2023) attributed this to low-level moisture flux convergence caused by the land breeze. Figure 9 indicates a stronger land breeze for DC-WITH-PROP than DC-NO-PROP. In figure 9a there is very faint convergence along the coast, with a very narrow convergence line that has propagated a few km offshore by 23 LT (figure 9b). Hence, even when the convection does not propagate offshore, there is still a land breeze. However, on days with propagation the convergence at the land breeze front is stronger, with a more intense convergence line seen in figure 9c. Comparing figures 9b and 9d we see that the land breeze has a similar strength in each

422 case, so the difference in convergence is due to the wind direction further offshore. This
 423 is directly mainly alongshore for DC-NO-PROP but towards the coast for DC-WITH-PROP.
 424 By the time the precipitation has spread around 30–40 km offshore at 23 LT (figure 9d)
 425 there is fairly strong convergence in the whole offshore region covered by rainfall. As in
 426 Peatman et al. (2023), however, it is not possible to determine to what extent this is caused
 427 by cold pools and there may also be a contribution due to convergent inflow into the con-
 428 vection itself.

429 Further to the above arguments, we consider the properties of air that flows into
 430 the storm as it propagates (that is, the storm-relative inflow) and ask what effect this
 431 has on the overall convective available potential energy (CAPE), to investigate why the
 432 conditions on DC-WITH-PROP days are particularly conducive to sustaining convection.
 433 Following Alfaro (2017) we compute the layer-lifting CAPE (CAPE_{ll}), which is the in-
 434 stability of inflowing air, averaged over the troposphere. The storm-relative inflow speed
 435 (whether from in front of or behind the storm, relative to its motion) is $|u_{\text{on}}(p) - \text{PS}|$,
 436 where u_{on} is the onshore wind speed and PS is the storm’s propagation speed, defined
 437 as positive onshore. As we consider air parcels flowing into the storm at all heights, the
 438 important measure of instability is $\text{CAPE}(p)$, the CAPE of an air parcel lifted from pres-
 439 sure level p . Then we define

$$440 \quad \text{CAPE}_{ll} = \frac{\int_{p_0}^{p_T} |u_{\text{on}}(p) - \text{PS}| \text{CAPE}(p) dp}{\int_{p_0}^{p_T} |u_{\text{on}}(p) - \text{PS}| dp}, \quad (3)$$

441 where p_T is the pressure level of the tropopause, taken to be 120 hPa. Where an air par-
 442 cel is convectively stable, we take $\text{CAPE}(p) = 0$ by definition. In practice, $\text{CAPE}(p) >$
 443 0 only in the lowest few km of the troposphere. We repeated all calculations using the
 444 alongshore flow u_{along} and found the alongshore contribution to be negligible (not shown).

445 From figure 4j we take $\text{PS} = -2.8 \text{ m s}^{-1}$ and compute CAPE_{ll} for the mean pro-
 446 file at each time of day on DC-WITH-PROP days. To test the sensitivity to the PS value,
 447 we repeated the calculation (not shown) using $\text{PS} = -3.5 \text{ m s}^{-1}$ and -1.8 m s^{-1} (the
 448 speeds of the fast and slow edges of the propagation envelope in figure 4j) and there were
 449 no substantial differences to the results. For simplicity, the calculation is carried out at
 450 a point location over the coastal city of Bengkulu (red dot in figure 2). By way of com-
 451 parison, we also compute CAPE_{ll} for a hypothetical propagating storm with the same
 452 PS on DC-NO-PROP days. The two curves are shown in figure 11a. For DC-WITH-PROP,

453 CAPE_{ll} peaks in the mid-late afternoon and early evening at around 4 times the value
 454 for DC-NO-PROP. Hence, the mean conditions for DC-WITH-PROP provide greater insta-
 455 bility to sustain propagating convection than would be provided on DC-NO-PROP days.

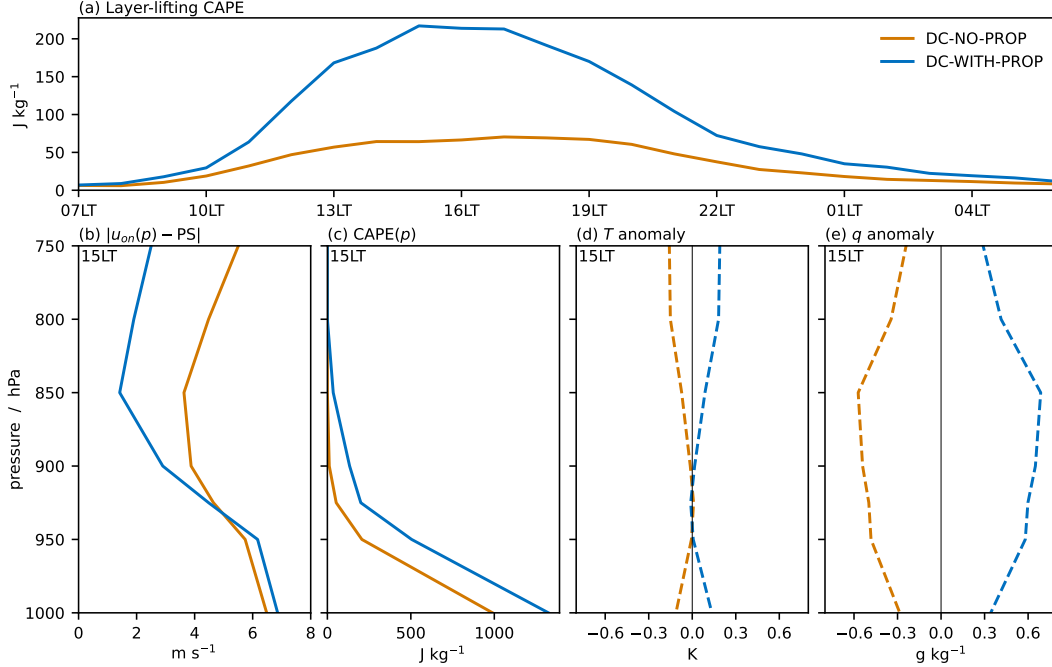


Figure 11. (a) Mean diurnal cycle of layer-lifting CAPE (see equation 3). Bottom row: mean profiles at 15 LT of (b) storm-relative onshore wind, $|u_{on}(p) - PS|$, (c) CAPE when an air parcel is lifted from pressure level p , (d) temperature anomaly and (e) specific humidity anomaly. In (d) and (e), the anomalies (indicated by dashed curves) are taken relative to the mean over all days with a diurnal cycle. Calculations are made for mean profiles at Bengkulu (red dot in figure 2).

456 Figures 11b,c show the two profiles involved in the integral in equation 3, $|u_{on}(p) - PS|$
 457 and $CAPE(p)$, at 15 LT, when $CAPE_{ll}$ peaks on DC-WITH-PROP days. Where $CAPE(p)$
 458 is large there is little difference between the two storm-relative wind speeds, whereas the
 459 larger difference in storm-relative inflow occurs only where $CAPE(p)$ is very small. Hence,
 460 it is the differences in low-level $CAPE(p)$ that have the greatest contribution to $CAPE_{ll}$.

461 The CAPE is determined by T and specific humidity q , shown as anomalies from
 462 all diurnal cycle days in figures 11d,e. By exchanging either the two T profiles or the two
 463 q profiles in the CAPE calculation, it is found that only the q makes a substantial dif-
 464 ference to the result (not shown). Hence, it is the low-level humidity that ultimately de-

465 terminates that high-instability air flows into propagating convection on DC-WITH-PROP
466 days.

467 In summary, a number of physical arguments may be made that are consistent with
468 only certain diurnal cycle days having offshore propagation of the convection. The mean
469 mid-level winds have a strong offshore component on DC-WITH-PROP days but are pre-
470 dominantly alongshore, with a slight onshore component, on DC-NO-PROP days, imply-
471 ing there is a steering flow that may begin the process of organized convection propa-
472 gating from the mountains towards the coast. The land breeze, which previous studies
473 have shown is important for the offshore propagation due to the low-level convergence
474 it provides, appears to be stronger on DC-WITH-PROP days, although there may also be
475 a contribution from cold pools that is not easy to diagnose from the model run used here,
476 as both the land breeze and cold pools are shallow density currents that merge and are
477 not easily distinguished. Finally, the mean low-level moisture around the coast on DC-
478 WITH-PROP days causes larger CAPE with respect to air parcels lifted from near the ground,
479 which contributes more instability to the storm as it propagates, sustaining the convec-
480 tion.

481 **4 Discussion and conclusion**

482 This study has considered the nocturnal offshore propagation of convection south-
483 west of Sumatra, seeking to understand, at a physical process level, why this phenomenon
484 occurs on some days and not others during DJF. Using a convection-permitting model
485 as a research tool, days were identified as having a diurnal cycle of precipitation over land
486 that propagates offshore overnight, a diurnal cycle but with no propagation, large-scale
487 rainfall instead of a diurnal cycle, or no rain at all. In agreement with previous studies
488 (Oh et al., 2012; Peatman et al., 2014; Sakaeda et al., 2017; Vincent & Lane, 2017; Sakaeda
489 et al., 2020; Peatman et al., 2021), the diurnal cycle is most likely to occur ahead of the
490 arrival of an active MJO envelope and the most suppressed local conditions, with little
491 or no rain, ahead of the suppressed MJO envelope. However, the MetUM simulation has
492 too many DC-NO-PROP days, at the expense of NONE. The diurnal cycle is slightly more
493 likely to occur over south-west Sumatra during El Niño or IOD+ than during La Niña
494 or IOD-. Days with large-scale rainfall and days with little or no rainfall are slightly
495 more likely to occur during La Niña or IOD-. However, all regimes may occur in any

496 phase of the MJO, ENSO or IOD, due to local conditions which exert the main control
 497 over the rainfall behaviour.

498 This research has demonstrated the dynamical and thermodynamical conditions
 499 responsible for each of the four regimes occurring on any given day. The schematic di-
 500 agram in figure 12 summarizes the results.

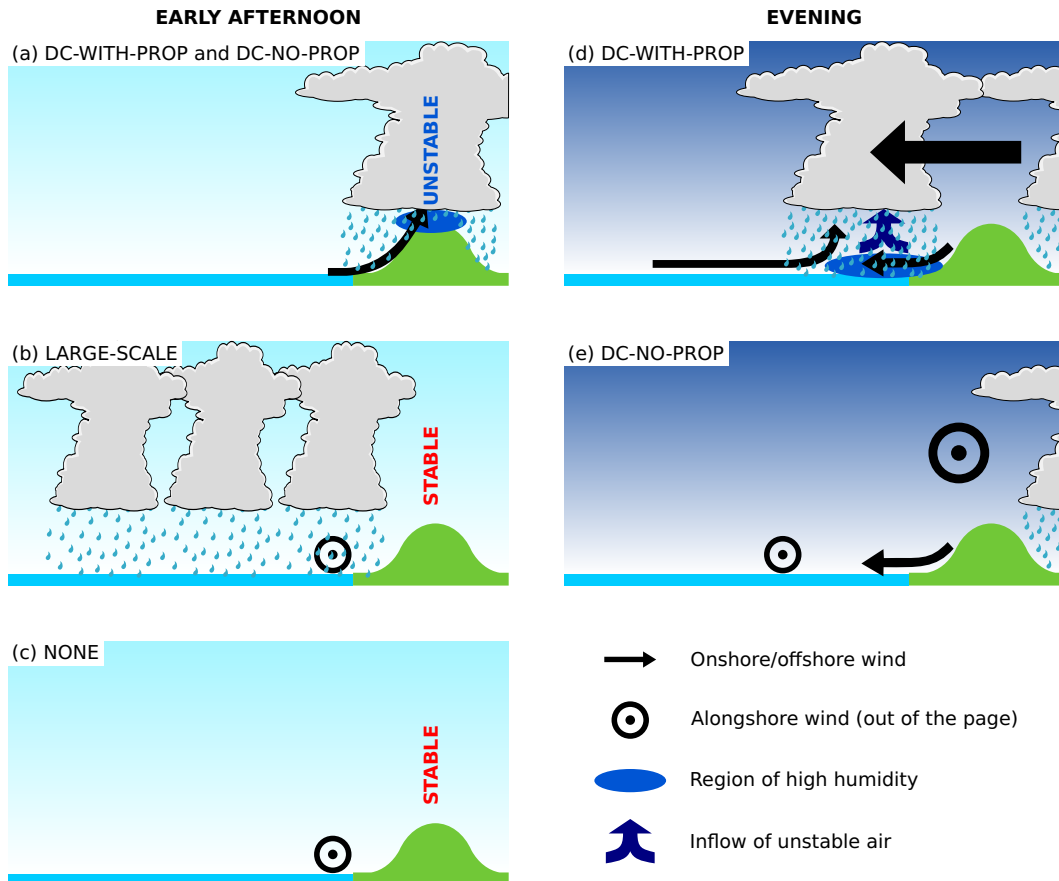


Figure 12. Schematic diagram showing conditions that occur in each of the regimes defined in table 1. Early afternoon: (a) days with a diurnal cycle, (b) LARGE-SCALE and (c) NONE. Evening: (d) DC-WITH-PROP and (e) DC-NO-PROP.

501 During the morning and up until the early afternoon, the local conditions deter-
 502 mine whether the deep convection over the mountains, that constitutes the Sumatra di-
 503 urnal cycle, will be triggered or not. On days with no diurnal cycle – whether there is
 504 large-scale rainfall (figure 12b) or no rainfall nearby (figure 12c) – the vertical profile over
 505 the mountains is stable against moist convection. On days with a diurnal cycle (figure 12a),
 506 a moist boundary layer over the mountains causes the vertical profile to be unstable, since

507 the higher humidity increases the low-level equivalent potential temperature. Moreover,
508 days with a diurnal cycle have stronger onshore winds, whereas on days with no diur-
509 nal cycle the large-scale flow is predominantly alongshore. The onshore, upslope flow pro-
510 vides low-level convergence over the mountains, allowing the triggering of convection in
511 the unstable conditions. The fact that these regimes are more likely to occur ahead (to
512 the east) of the active MJO is in agreement with Birch et al. (2016) who showed that
513 the sea breeze circulation is responsible for local-scale convective triggering ahead of the
514 MJO. However, more research would be required to understand exactly why the onshore
515 sea breeze and low-level humidity are more often associated with El Niño than La Niña,
516 and IOD+ than IOD-.

517 Understanding the local conditions associated with each regime should in princi-
518 ple assist in forecasting, at least on the day in question and possibly in advance, whether
519 an intense diurnal cycle of convection will occur. However, while local conditions dur-
520 ing the morning determine the occurrence of the diurnal cycle, they do not determine whether
521 that convection will later propagate offshore.

522 The important differences in the local conditions do not emerge until the afternoon
523 and evening (figures 12d,e). The wind at mid-levels is predominantly offshore on days
524 with offshore propagation, suggesting it acts as a steering flow as the convection migrates
525 from the mountain peaks to the coast. When there is no offshore propagation, the mid-
526 level wind is predominantly alongshore (from the north-west). However, Peatman et al.
527 (2023) showed the importance of low-level moisture flux convergence due to offshore-propagating
528 density currents (see section 1) for the propagation of the squall line. Here we find that
529 the land-sea breeze circulation is evident on days with and without the offshore prop-
530 agation of convection, but the wind direction further offshore causes stronger low-level
531 convergence on days with the offshore propagation. Furthermore, due to low-level hu-
532 midity around the coast, when the convection propagates offshore, the storm-relative in-
533 flow of low-level air contributes further instability (CAPE), helping to maintain the con-
534 vection as it propagates. On days without offshore propagation the coastal low-level hu-
535 midity is less, so that a storm propagating at the same speed would have less instabil-
536 ity added by the storm-relative inflow. Taken together, all these differences between the
537 two regimes present a picture of how the physical mechanisms governing the occurrence
538 of the propagation vary between days.

539 Peatman et al. (2023) noted a difficulty in the analysis of density currents that com-
540 prise the land-sea breeze circulation, namely that cold pools caused by evaporation of
541 rainfall also propagate as density currents, and it is not simple to distinguish the two.
542 In the simulations we use here, the same problem occurs, so we must acknowledge that
543 the relative importance of the land breeze and cold pools, in providing the low-level con-
544 vergence that forces convection to develop progressively offshore, remains unknown. Fu-
545 ture work will use simulations that include a tracer, generated where there is evapora-
546 tion and subsequently advected around, to quantify the contribution of cold pools to the
547 convergence.

548 A further limitation of the present study is that, although low-level humidity is found
549 to cause the instability responsible for the diurnal convection over the mountains and
550 the higher-CAPE air flowing into the convection as it propagates, it is not clear what
551 controls this low-level humidity. Analysis not shown here indicates that there is no sin-
552 gle cause of this humidity variability, with possible roles for interannual variability and
553 a build-up of humidity over a timescale of 2–3 days, possibly due to evapotranspiration.
554 However, quantifying the various contributions to the humidity is beyond the scope of
555 this study, so further investigation is required.

556 Notwithstanding these limitations, the present study builds on existing work to aid
557 understanding of how local diurnal cycle and propagation behaviour arises from dynam-
558 ical and thermodynamical conditions, with potential benefits for forecasters and model
559 developers. State-of-the-art global models are still typically run on grids that cannot re-
560 solve coastal processes well, so accurate parametrizations such as land-sea breeze schemes
561 are of great importance to the modelling community. Work such as the present study
562 gives insights into the coastal processes that must be parametrized. This study also demon-
563 strates the power of a convolutional neural network in automating the identification of
564 regimes of coastal precipitation behaviour, provided there is a large enough training data
565 available. Future work may generalize the results of this study by applying a pre-trained
566 machine learning model to coastlines across the global tropics.

567 We note also that low-level humidity is a major control on the diurnal cycle and
568 its offshore propagation. The next generation of geostationary satellites will provide low-
569 level humidity observations at high spatial and temporal resolution, using infrared sounders
570 (e.g., ESA, 2023). The results of this study provide an example of the value of assim-

571 ilating these observations into models, given the impact on convection and, therefore,
572 on high-impact precipitation.

573 **Open Research Section**

574 Raw and processed model data are available along with analysis code at [https://](https://doi.org/10.5281/zenodo.13747261)
575 doi.org/10.5281/zenodo.13747261 (Peatman et al., 2024).

576 GPM IMERG precipitation (Huffman et al., 2019) is available from the National
577 Aeronautics and Space Administration (NASA) Goddard Earth Sciences Data and In-
578 formation Services Center (GES DISC; [https://pmm.nasa.gov/data-access/downloads/](https://pmm.nasa.gov/data-access/downloads/gpm)
579 [gpm](https://pmm.nasa.gov/data-access/downloads/gpm)). RMM indices are available from the Bureau of Meteorology (BoM, 2024, [www.bom](http://www.bom.gov.au/climate/mjo/graphics/rmm.74toRealtime.txt)
580 [.gov.au/climate/mjo/graphics/rmm.74toRealtime.txt](http://www.bom.gov.au/climate/mjo/graphics/rmm.74toRealtime.txt)). GLOBE orography (Hastings
581 et al., 1999) is available from the National Oceanic and Atmospheric Administration (NOAA;
582 <https://www.ngdc.noaa.gov/mgg/topo/globe.html>).

583 **Acknowledgments**

584 This research was funded by the National Environment Research Council (NERC) through
585 the TerraMaris project, grants NE/R016739/1, NE/R016704/1 and NE/R016712/1. JS
586 was funded by the Met Office Weather and Climate Science for Service Partnership (WC-
587 SSP) Southeast Asia. SJW was also supported by the National Centre for Atmospheric
588 Science, a NERC collaborative centre.

589 Data analysis was carried out using the Python *iris* package, version 3.3.1 (Iris
590 Contributors, 2022). The CNN was created using the Python *keras* package, version 2.11.0
591 (Chollet et al., 2015).

592 We thank Thi Lan Dao and Dr Bethan White for their feedback on this manuscript;
593 and Dr Claire Vincent and two anonymous reviewers, for their comments which improved
594 the manuscript prior to publication.

595 **References**

- 596 Alfaro, D. A. (2017). Low-Tropospheric Shear in the Structure of Squall Lines:
597 Impacts on Latent Heating under Layer-Lifting Ascent. *Journal of the Atmo-*
598 *spheric Sciences*, *74*(1), 229–248. doi: 10.1175/JAS-D-16-0168.1
599 Aoki, S., & Shige, S. (2024). Control of Low-Level Wind on the Diurnal Cycle of

- 600 Tropical Coastal Precipitation. *Journal of Climate*, *37*(1), 229–247. doi: 10
601 .1175/JCLI-D-23-0180.1
- 602 Biasutti, M., Yuter, S. E., Burleyson, C. D., & Sobel, A. H. (2012). Very high
603 resolution rainfall patterns measured by TRMM precipitation radar: Sea-
604 sonal and diurnal cycles. *Climate Dynamics*, *39*(1–2), 239–258. doi:
605 10.1007/s00382-011-1146-6
- 606 Birch, C. E., Webster, S., Peatman, S. C., Parker, D. J., Matthews, A. J., Li, Y.,
607 & Hassim, M. E. E. (2016). Scale interactions between the MJO and the
608 western Maritime Continent. *Journal of Climate*, *29*(7), 2471–2492. doi:
609 10.1175/JCLI-D-15-0557.1
- 610 BoM. (2024). *Realtime Multivariate MJO indices [Dataset]*. Retrieved from [http://](http://www.bom.gov.au/clim_data/IDCKGEM000/rmm.74toRealtime.txt)
611 www.bom.gov.au/clim_data/IDCKGEM000/rmm.74toRealtime.txt
- 612 Bush, M., Boutle, I., Edwards, J., Finnenkoetter, A., Franklin, C., Hanley, K., ...
613 Weeks, M. (2023). The second Met Office Unified Model-JULES Regional
614 Atmosphere and Land configuration, RAL2. *Geoscientific Model Development*,
615 *16*(6), 1713–1734. doi: 10.5194/gmd-16-1713-2023
- 616 Chollet, F., et al. (2015). *Keras*. <https://keras.io>.
- 617 ESA. (2023). *MTG (Meteosat Third Generation)*. Retrieved from [https://](https://www.eoportal.org/satellite-missions/meteosat-third-generation)
618 www.eoportal.org/satellite-missions/meteosat-third-generation (Ac-
619 cessed: 5 September 2024)
- 620 Fujita, M., Takahashi, H. G., & Hara, M. (2013). Diurnal cycle of precipitation
621 over the eastern Indian Ocean off Sumatra Island during different phases of
622 Indian Ocean Dipole. *Atmospheric Science Letters*, *14*(3), 153–159. doi:
623 10.1002/asl2.432
- 624 Garcia-Carreras, L., Parker, D. J., & Marsham, J. H. (2011). What is the Mecha-
625 nism for the Modification of Convective Cloud Distributions by Land Surface-
626 Induced Flows? *Journal of the Atmospheric Sciences*, *68*(3), 619–634. doi:
627 10.1175/2010JAS3604.1
- 628 Hastings, D. A., Dunbar, P. K., Elphinstone, G. M., Bootz, M., Murakami, H.,
629 Maruyama, H., ... MacDonald, J. S. (1999). *The Global Land One-kilometer*
630 *Base Elevation (GLOBE) digital elevation model, version 1.0 [Dataset]*. Re-
631 trieved from <http://www.ngdc.noaa.gov/mgg/topo/globe.html>
- 632 Hendon, H. H. (2003). Indonesian Rainfall Variability: Impacts of ENSO and Local

- 633 Air-Sea Interaction. *Journal of Climate*, 16(11), 1775–1790. doi: 10.1175/1520
634 -0442(2003)016(1775:IRVIOE)2.0.CO;2
- 635 Hersbach, H., Bell, B., Berrisford, P., Hirahara, S., Horányi, A., Muñoz-Sabater, J.,
636 ... Thépaut, J. (2020). The ERA5 global reanalysis. *Quarterly Journal of the*
637 *Royal Meteorological Society*, 146(730), 1999–2049. doi: 10.1002/qj.3803
- 638 Houze, R. A., Geotis, S. G., Marks, F. D., & West, A. K. (1981). Winter monsoon
639 convection in the vicinity of north Borneo. Part I: Structure and time variation
640 of the clouds and precipitation. *Monthly Weather Review*, 109(8), 1595–1614.
641 doi: 10.1175/1520-0493(1981)109(1595:WMCITV)2.0.CO;2
- 642 Howard, E., Woolnough, S., Klingaman, N., Shipley, D., Sanchez, C., Peatman,
643 S. C., ... Matthews, A. J. (2024). Evaluation of multi-season convection-
644 permitting atmosphere - mixed-layer ocean simulations of the Maritime
645 Continent. *Geoscientific Model Development*, 17(9), 3815–3837. doi:
646 10.5194/gmd-17-3815-2024
- 647 Huffman, G. J., Stocker, E. F., Bolvin, D. T., Nelkin, E. J., & Tan, J. (2019).
648 *GPM IMERG Final Precipitation L3 Half Hourly 0.1 degree x 0.1 degree V06*
649 *[Dataset]*. doi: 10.5067/GPM/IMERG/3B-HH/06
- 650 Iris Contributors. (2022). *Iris*. Retrieved from <https://github.com/SciTools/iris>
651 doi: 10.5281/zenodo.595182
- 652 Kurniadi, A., Weller, E., Min, S.-K., & Seong, M.-G. (2021). Independent ENSO
653 and IOD impacts on rainfall extremes over Indonesia. *International Journal of*
654 *Climatology*, 41(6), 3640–3656. doi: 10.1002/joc.7040
- 655 Large, W. G., McWilliams, J. C., & Doney, S. C. (1994). Oceanic vertical mixing: A
656 review and a model with a nonlocal boundary layer parameterization. *Reviews*
657 *of Geophysics*, 32(4), 363–403. doi: 10.1029/94RG01872
- 658 Love, B. S., Matthews, A. J., & Lister, G. M. S. (2011). The diurnal cycle of pre-
659 cipitation over the Maritime Continent in a high-resolution atmospheric model.
660 *Quarterly Journal of the Royal Meteorological Society*, 137, 934–947. doi:
661 10.1002/qj.809
- 662 Mapes, B. E., Warner, T. T., & Xu, M. (2003). Diurnal patterns of rainfall in
663 northwestern South America. Part III: Diurnal gravity waves and noctur-
664 nal convection offshore. *Monthly Weather Review*, 131(5), 830–844. doi:
665 10.1175/1520-0493(2003)131(0830:DPORIN)2.0.CO;2

- 666 Mapes, B. E., Warner, T. T., Xu, M., & Negri, A. J. (2003). Diurnal pat-
 667 terns of rainfall in northwestern South America. Part I: Observations
 668 and context. *Monthly Weather Review*, *131*(5), 799–812. doi: 10.1175/
 669 1520-0493(2003)131(0799:DPORIN)2.0.CO;2
- 670 Montserrat, D. M., Lin, Q., Allebach, J., Delp, E. J., Lin, Q., Allebach, J., &
 671 Delp, E. J. (2017). Training Object Detection And Recognition CNN
 672 Models Using Data Augmentation. *Electronic Imaging*, *29*, 27–36. doi:
 673 10.2352/ISSN.2470-1173.2017.10.IMAWM-163
- 674 Mori, S., Jun-Ichi, H., Tauhid, Y. I., & Yamanaka, M. D. (2004). Diurnal land-sea
 675 rainfall peak migration over Sumatera Island, Indonesian Maritime Continent,
 676 observed by TRMM satellite and intensive rawinsonde soundings. *Monthly*
 677 *Weather Review*, *132*(8), 2021–2039. doi: 10.1175/1520-0493(2004)132(2021:
 678 DLRPMO)2.0.CO;2
- 679 Oh, J. H., Kim, K. Y., & Lim, G. H. (2012). Impact of MJO on the diurnal cycle
 680 of rainfall over the western Maritime Continent in the austral summer. *Climate*
 681 *Dynamics*, *38*(5–6), 1167–1180. doi: 10.1007/s00382-011-1237-4
- 682 Peatman, S. C., Birch, C., Schwendike, J., Marsham, J., Howard, E., Woolnough, S.,
 683 ... Matthews, A. (2024). *Physical controls on the variability of offshore propa-*
 684 *gation of convection from Sumatra [Dataset]*. doi: 10.5281/zenodo.13747262
- 685 Peatman, S. C., Birch, C. E., Schwendike, J., Marsham, J. H., Dearden, C., Webster,
 686 S., ... Matthews, A. J. (2023). The Role of Density Currents and Gravity
 687 Waves in the Offshore Propagation of Convection over Sumatra. *Monthly*
 688 *Weather Review*, *151*(7), 1757–1777. doi: 10.1175/MWR-D-22-0322.1
- 689 Peatman, S. C., Matthews, A. J., & Stevens, D. P. (2014). Propagation of the
 690 Madden-Julian Oscillation through the Maritime Continent and scale inter-
 691 action with the diurnal cycle of precipitation. *Quarterly Journal of the Royal*
 692 *Meteorological Society*, *140*(680), 814–825. doi: 10.1002/qj.2161
- 693 Peatman, S. C., Schwendike, J., Birch, C. E., Marsham, J. H., Matthews, A. J., &
 694 Yang, G.-Y. (2021). A Local-to-Large Scale View of Maritime Continent
 695 Rainfall: Control by ENSO, MJO, and Equatorial Waves. *Journal of Climate*,
 696 *34*(22), 8933–8953. doi: 10.1175/JCLI-D-21-0263.1
- 697 Poojary, R., Raina, R., & Mondal, A. K. (2021). Effect of data-augmentation on
 698 fine-tuned CNN model performance. *IAES International Journal of Artificial*

- 699 *Intelligence (IJ-AI)*, 10(1), 84–92. doi: 10.11591/ijai.v10.i1.pp84-92
- 700 Qian, J.-H. (2008). Why precipitation is mostly concentrated over islands in the
701 Maritime Continent. *Journal of the Atmospheric Sciences*, 65(4), 1428–1441.
702 doi: 10.1175/2007JAS2422.1
- 703 Ramage, C. S. (1968). Role of a Tropical “Maritime Continent” in the atmospheric
704 circulation. *Monthly Weather Review*, 96(6), 365–370. doi: 10.1175/1520
705 -0493(1968)096<0365:ROATMC>2.0.CO;2
- 706 Rauniyar, S. P., & Walsh, K. J. E. (2013). Influence of ENSO on the diurnal cycle of
707 rainfall over the Maritime Continent and Australia. *Journal of Climate*, 26(4),
708 1304–1321. doi: 10.1175/JCLI-D-12-00124.1
- 709 Sakaeda, N., Kiladis, G., & Dias, J. (2020). The diurnal cycle of rainfall and the
710 convectively coupled equatorial waves over the Maritime Continent. *Journal of*
711 *Climate*, 33(8), 3307–3331. doi: 10.1175/JCLI-D-19-0043.1
- 712 Sakaeda, N., Kiladis, G. N., & Dias, J. (2017). The diurnal cycle of tropical cloudi-
713 ness and rainfall associated with the Madden-Julian Oscillation. *Journal of*
714 *Climate*, 30(11), 3999–4020. doi: 10.1175/JCLI-D-16-0788.1
- 715 Shorten, C., & Khoshgoftaar, T. M. (2019). A survey on Image Data Augmentation
716 for Deep Learning. *Journal of Big Data*, 6(1), 60. doi: 10.1186/s40537-019
717 -0197-0
- 718 Stuecker, M. F., Timmermann, A., Jin, F.-F., Chikamoto, Y., Zhang, W., Witten-
719 berg, A. T., ... Zhao, S. (2017). Revisiting ENSO/Indian Ocean Dipole
720 phase relationships. *Geophysical Research Letters*, 44(5), 2481–2492. doi:
721 10.1002/2016GL072308
- 722 Vincent, C. L., & Lane, T. P. (2017). A 10-year austral summer climatology
723 of observed and modeled intraseasonal, mesoscale, and diurnal variations
724 over the Maritime Continent. *Journal of Climate*, 30(10), 3807–3828. doi:
725 10.1175/JCLI-D-16-0688.1
- 726 Webster, P. J., & Hoyos, C. D. (2004). Prediction of Monsoon Rainfall and River
727 Discharge on 15-30-Day Time Scales. *Bulletin of the American Meteorological*
728 *Society*, 85(11), 1745–1765. doi: 10.1175/BAMS-85-11-1745
- 729 Yang, G.-Y., & Slingo, J. M. (2001). The Diurnal Cycle in the Tropics. *Monthly*
730 *Weather Review*, 129(1994), 784–801. doi: 10.1175/1520-0493(2001)129<0784:
731 TDCITT>2.0.CO;2